Adsorption equilibrium of nitrogen dioxide in porous materials

Matito-Martos, I.; Rahbari, A.; Martin-Calvo, A.; Dubbeldam, D.; Vlugt, T. J.H.; Calero, S

Important note
To cite this publication, please use the final published version (if applicable).
Please check the document version above.

ADSORPTION EQUILIBRIUM OF NITROGEN DIOXIDE IN POROUS MATERIALS

I. Matito-Martos[a], A. Rahbari[b], A. Martin-Calvo[c], D. Dubbeldam[d], T.J.H. Vlugt[b], and S. Calero[*a]

[a]*Department of Physical, Chemical and Natural Systems, University Pablo de Olavide, Sevilla 41013, Spain*
[b]*Process and Energy Department, Delft University of Technology, Leeghwaterstraat 39, 2628CB Delft, The Netherlands*
[c]*Department of Chemical Engineering, Vrije Universiteit Brussel, Brussels, 1050, Belgium*
[d]*Van 't Hoff Institute for Molecular Sciences, University of Amsterdam, Science Park 904, 1098XH Amsterdam, The Netherlands*

Abstract

The effect of confinement on the equilibrium reactive system containing nitrogen dioxide and dinitrogen tetroxide is studied by molecular simulation and the reactive Monte Carlo (RxMC) approach. Bulk-phase reaction was successfully reproduced and five all-silica zeolites (i.e. FAU, FER, MFI, MOR, and TON) with different topologies were selected to study their adoption behavior. Dinitrogen tetroxide showed stronger affinity than nitrogen dioxide in all zeolites due to size effects, but exclusive adsorption sites in MOR allowed the adsorption of nitrogen dioxide with no competition at these sites. From the study of adsorption isotherms and isobars of the reacting mixture, confinement enhanced the formation of dimers in the full range of pressure and temperature, finding the largest deviations from bulk fractions at low temperature and high pressure. Channel size and shape of the zeolite have a noticeable influence on dinitrogen tetroxide formation, being more important in MFI, closely followed by TON and MOR, and finally FER and FAU. Preferential adsorption sites in MOR lead to an unusual strong selective adsorption towards nitrogen dioxide, demonstrating that the topological structure has a crucial influence on the composition of the mixture and must be carefully considered in systems containing nitrogen dioxide.

Introduction

Nitrogen oxides (NO$_x$) refer to a mixture of compounds containing nitrogen and oxygen. However, this term usually refers to NO, NO$_2$, and N$_2$O, due to their larger relative amount and the fact that the others are unstable and do not appear in the atmosphere.[1,2] Dinitrogen oxide (N$_2$O) is a non-toxic gas that mainly comes from the natural microbial denitrification of organic matter.[3] Conversely, the source of nitrogen monoxide (NO) and nitrogen dioxide (NO$_2$) is mainly anthropogenic, being produced in combustion processes, especially at high temperature. Internal combustion engines are their most important sources[4] along with thermal power stations.[5] In these processes, excess air used to complete the combustion leads to formation of NOx in the combustion products. In addition, nitrogen oxides are intermediates in some chemical processes such as the fabrication of nitric acid, paints, nitration of organic chemicals, manufacture of explosives, or as rocket fuels.[1] NO and NO$_2$ have a high reactivity with oxygen from air, being of capital importance in atmospheric chemistry. These gases are the main precursors of tropospheric ozone and other secondary pollutants when they react with oxide volatile organic compounds in presence of sun light. They are also responsible from acid rain when combined with water vapor.[6,7] The release of NO$_x$ from combustion also favors photochemical reactions deriving to the well-known photochemical smog. Additionally, nitrogen oxides are toxic to human inhalation.

The important effects on the environment and human health, along with increasing pollution, leads to the establishment of more restrictive levels of emissions and the need of appropriate methods to reduce and control the emissions of nitrogen oxides. In order to achieve this aim, there are two main approaches. One focuses on the combustion process itself trying to reduce the amount of NO$_x$ produced. This type of solution achieves

ratios of decomposition below 50% in most cases.[8] The second strategy is based on post-combustion solutions focused on the capture and removal of NO_x after being produced from the combustion products. Among different methods, Selective Catalytic Reduction (SCR) is one of the solutions with higher decomposition ratios while no wastes are produced.[8,9] The capture and removal of NO and NO_2 is not only an interesting subject itself but also has importance in Carbon dioxide Capture and Storage processes (CCS). Traces of NO_x and other gases such as sulphur oxides (SO_x) strongly influence the capture and removal of CO_2. [10–13] As an alternative technology for the removal of NO_x and other pollutants with a better efficiency than SCR processes, adsorption in porous materials is an interesting option. With this method, wastes are not produced and energy requirements are low.[13–16] The key point for the capture and removal of targeted pollutants is the identification of suitable materials and operation conditions. Zeolites have been proved to be efficient molecular sieves for the capture, separation, and purification of mixtures containing small gas molecules.[13,17,18] These materials exhibit many interesting properties such as large variety of pore size and shape or high thermal stability.[19] Zeolites consist of basic tetrahedral units, in which a central T-atom (usually silicon) is bonded to four oxygen atoms. The basic units are connected generating 3D structures with a huge variety of topologies (i.e. cages and/or channels with different directionality) whose effect in the adsorption performance is difficult to screen experimentally. The large amount of available zeolite topologies[20] gives to molecular simulations a capital importance as a powerful tool to evaluate the performance of porous material and gases at a molecular level with a low cost associated.[21–23]

Simulating systems containing nitrogen monoxide and nitrogen dioxide becomes challenging as these gases co-exist as an equilibrium mixture of their monomer and dimer,

depending on temperature and pressure conditions. The properties of the equilibrium mixtures NO/N$_2$O$_2$ and NO$_2$/N$_2$O$_4$ have been extensively studied experimentally and theoretically.[24–36] For both equilibrium reactions, association is favored at higher values of pressure and low temperature, following Le Chatelier's principle for endothermic dissociation reactions. In the case of the NO/N$_2$O$_2$ equilibrium mixture, the fraction of dimer in the gas phase is very small (less than 3% at temperature below 180 K and room pressure), and therefore its contribution can be neglected at temperatures above room temperature.[25,26] The NO$_2$/N$_2$O$_4$ reaction was studied by James and Marshal in liquid and solid states, reporting equilibrium constants from 77 to 295 K with N$_2$O$_4$ fractions larger than 0.99 at temperatures between 250-295 K (strong association in the liquid phase).[33] Gas phase reaction was studied by Chao et $al.$,[32] Yoshino et $al.$,[30] Verhoek et $al.$,[31] and Harris and Kenneth,[37] among others. These studies show a NO$_2$ mole fraction in the vapor phase of around 0.9 at 373.15 K and complete dissociation at 413.15 K. The mole fraction of dinitrogen tetroxide rapidly decreases as pressure decreases or temperature increases. However, dimerization can also occur in the gas phase.[32] Thus, a $priori$, dimers must be considered when considering systems containing NO$_2$ in operation conditions near to room pressure and temperature. On the other hand, properties of gases and liquids adsorbed in narrow pores highly differ from these in the bulk phase. In this regard, the reactive Monte Carlo (RxMC) method, independently developed by Johnson et $al.$[38] and Smith and Triska[39] for modelling chemical reactions at equilibrium, has been already applied to reactive equilibrium studies,[40] including a) simple bulk phase reactions,[41–44] b) combined chemical and phase equilibria,[38,45] and c) reactions in confined systems,[41,46–48] among others. In this method, a chemical reaction in a system of interacting molecules is modeled as a Monte Carlo trial move. In one of the initial studies in the literature that used the RxMC method to determine the composition of a given reaction in a confined

geometry, Borówko and Zagórski examined the conversion of a LJ dimerisation reaction within a model pore.[46] Independently, Turner *et al.* simulated the equilibrium conversion of the ammonia synthesis reaction and the NO dimerisation reaction within a model carbon pore.[41] In these works, the conversion of the reactions in the pore deviated significantly from bulk-phase composition , and a strong effect of the pore width was found. Mullen and Maginn recently modeled xylene isomer mixture in a carbon nanotube, finding strong dependence between the dominant xylene isomer and the nanotube diameter.[49] The role of the pore structure was more deeply studied by Hansen *et al.* in zeolites for the propene metathesis reaction system.[47,48] They also found significant increases in the pore phase conversion compared to bulk-phase as well as a strong influence of the zeolite topology, temperature and pressure on the pore-phase composition.

Here, we study the effect of confinement on the equilibrium mixture nitrogen dioxide/dinitrogen tetroxide (NO_2/N_2O_4), at different operation conditions of pressure and temperature. We provide insights to understand at a molecular level how the pore structure of the materials modifies the mixture composition by selecting five pure silica zeolites with different topology: One with cages separated by windows (FAU) and four with intersected channels and different channel size and directionality (MOR, TON, FER, and MFI). The information given in this paper is organized as follows. Simulation techniques and models for adsorbates and frameworks are detailed in the next section. In section 3, we discuss the results obtained from the study of the adsorption performance of both species as pure component and binary mixtures, looking in the structural features that difference the selected materials. Finally, we provide some concluding remarks in the last section.

Methodology

We use the reactive Monte Carlo method (RxMC) to simulate equilibrium properties of the reactive system containing nitrogen dioxide and dinitrogen tetroxide, both in the bulk-phase and confined in FAU, FER, TON, MFI, and MOR zeolites. RxMC samples forward and reverse reaction steps in addition to conventional MC trial moves. The method requires only the input of the full isolated molecule partition functions[38] for the reactants and products (or Gibbs-free energies of formation of isolated molecules),[39] along with the usual ensemble constants and intermolecular interaction potentials.

The ideal gas partition function for a general case of non-linear polyatomic molecule is defined[50] as

$$q(V,T) = \left(\frac{2\pi M k_B T}{h^2}\right)^{3/2} V \cdot \frac{\pi^{1/2}}{\sigma}\left(\frac{T^3}{\Theta_{rot,A}\Theta_{rot,B}\Theta_{rot,C}}\right)^{1/2} \cdot \left(\prod_{j=1}^{3n-6}\frac{1}{1-\exp(-\Theta_{vib,j}/T)}\right) \cdot g_{e1}\exp(D_0/k_B T)$$

(1)

$\Theta_{rot,A}$, $\Theta_{rot,B}$, and $\Theta_{rot,C}$, are the characteristic rotational constants of the molecule. M denotes mass of the molecule, $\Theta_{vib,j}$, is the characteristic vibrational temperature corresponding to normal mode j, D_0 is the atomization energy at 0 K, σ is the rotational symmetry number or external symmetry number of the molecule.[50] Since only the temperature dependent part of the partition function is needed, dividing eq. 1 by volume, we obtain

$$\hat{q}(T) = \frac{q(V,T)}{V} = \left(\frac{2\pi M k_B T}{h^2}\right)^{3/2} \cdot \frac{\pi^{1/2}}{\sigma}\left(\frac{T^3}{\Theta_{rot,A}\Theta_{rot,B}\Theta_{rot,C}}\right)^{1/2} \cdot \left(\prod_{j=1}^{3n-6}\frac{1}{1-\exp(-\Theta_{vib,j}/T)}\right) \cdot g_{e1}\exp(D_0/k_B T)$$

(2)

This expression can be rearranged and defined in terms of $\hat{q}_0(T)$, an ideal gas partition function (excluding the volume term) in which the ground state energy is zero:

$$\hat{q}(T) = \hat{q}_0(T) \exp(D_0/k_B T) \tag{3}$$

In order to compute the ideal gas partition function, rotational and vibrational constants can be obtained either from ab initio quantum calculations or from experimental data available in literature, or alternatively from JANAF thermochemical tables.[47,50–54] The ideal gas partition functions of nitrogen dioxide and dinitrogen tetroxide used in this study are obtained based on frequency analysis on optimized molecular geometries in Gaussian09 at mp2 level of theory with 6-311+G(2d,2p) basis set.[55] Ideal gas partition functions obtained from ab initio calculations are then compared with the ones obtained based on experimental vibrational and rotational frequencies of nitrogen oxide and nitrogen tetroxide.[56–61] JANAF thermochemical tables are also used to obtain the ideal gas partition functions.[50,62] The atomization energy of a molecule D_0 can be determined from heats of formation at 0 K[47] and is summarized in Table 1. The temperature dependent part of the ideal gas partition functions ($\hat{q}_0(T)$) obtained from all three methods are in excellent agreement and are summarized in Table 2. More details about the RxMC method can be found elsewhere.[39–41,51]

Table 1 Atomization energies of nitrogen oxide and dinitrogen tetroxide determined based on heats of formation at 0 K from JANAF tables.[63]

	D_0 [kJ · mol^{-1}]
NO$_2$	928.47
N$_2$O$_4$	1910.10

Table 2 Computed temperature dependent part of the ideal gas partition functions (zero ground state energy), as defined in eq. 2 and 3, based on quantum computations using Gaussian09 (mp2/6-311+G(2d,2p)), experimental values from literature and JANAF tables.

	$\hat{q}_0(T)$ NO_2 /[Å^{-3}]			$\hat{q}_0(T)$ N_2O_4 /[Å^{-3}]		
T (K)	Gaussian	literature	JANAF	Gaussian	literature	JANAF
273.1	1.0757E+06	1.0611E+06	1.0636E+06	1.4386E+08	1.3349E+08	1.6113E+08
298.2	1.4108E+06	1.3931E+06	1.3949E+06	2.3786E+08	2.1827E+08	2.6125E+08
318.1	1.7261E+06	1.7060E+06	1.7066E+06	3.4931E+08	3.1801E+08	3.7747E+08
359.6	2.5396E+06	2.5160E+06	2.5149E+06	7.4668E+08	6.7010E+08	7.8575E+08
374.7	2.8944E+06	2.8705E+06	2.8678E+06	9.7251E+08	8.6881E+08	1.0142E+09
404.0	3.6867E+06	3.6646E+06	3.6572E+06	1.5999E+09	1.4180E+09	1.6404E+09

To check the correct reproduction of the single-phase bulk composition of the NO_2/N_2O_4 reaction system, simulations in the isobaric-isothermal ensemble have been carried out in combination with reaction sampling (RxMC). Simulations started with 200 NO_2 and 100 N_2O_4 molecules in the system and different conditions of temperature (from 273 to 400 K) and pressure (from 10^1 to $5 \cdot 10^2$ kPa). Monte Carlo trials performed during the simulations were translation, rotation, reinsertions, volume changes, and reaction sampling.[64] Results were obtained after running 25,000 equilibration and 250,000 production cycles. The number of Monte Carlo steps per cycle equals the total number of molecules initially in the system. The performance of the NO_2/N_2O_4 equilibrium mixture under confinement in porous materials is evaluated by Monte Carlo simulations in the Grand-Canonical ensemble (GCMC) with and without combination with reaction sampling (RxMC). The extension of the RxMC to confined system is well established, and this essentially only adds a classical external field to the system.[38,40,41,48,54] The energy levels of molecules are hardly effected by inter-molecular interactions or this external field at all. A fully explanation of the RxMC method and its applications can be found in the new edition of Allen and Tildesley.[65]

In GCMC simulations temperature and volume are fixed and a bulk-phase reservoir, represented by a fixed chemical potential, is in chemical equilibrium with the pore phase. The chemical potential directly relates to fugacity and fugacity to pressure by the fugacity coefficient through the Peng–Robinson equation of state.[64] For low pressures (ideal gas behavior), the fugacity equals the pressure. The number of cycles used are 50,000 and 500,000 for equilibration and production, respectively. The MC trial moves employed were translation, rotation, reinsertion, swap from the reservoir, and identity change for mixtures. Reaction sampling move was also used in these simulations including the RxMC approach. As in the work of Hansen et $al.$,[47] the RxMC method in the constant pressure Gibbs ensemble (GE-NPT) was also employed along with the reactive GCMC approach to ensure that in our system both approaches for modeling chemical equilibrium also lead to the same results. GE-NPT simulations started with 350–500 NO_2 molecules in the bulk-phase box and an empty pore phase (zeolite). We used the same number of cycles as in GCMC simulations. The same MC trials are also used, but eliminating identity changes and using transfer trials between simulation boxes (bulk and pore phase, respectively). All simulations are performed using the simulation code RASPA.[66,67]

Guest-host and guest-guest interactions are described by electrostatic and van der Waals interactions. Electrostatic interactions are considered by using Coulombic potentials and the Ewald summation method.[64] Van der Waals interactions are described by 12-6 Lennard-Jones potentials. A cutoff distance of 14 Å is used, where interactions are truncated and shifted with tail corrections applied. Nitrogen oxide monomer (NO_2) and dimer (N_2O_4) are modeled according to previous rigid models developed by Bourasseau et $al.$[29] Regarding the framework atoms, we use partial charges and Lennard-

Jones parameters from TraPPE-zeo forcefield.[68] Cross interactions are calculated by the Lorentz–Berthelot mixing rules.[69] Partial charges and Lennard-Jones parameters used in this work are collected in Table 3.

Table 3 Lennard-Jones parameters and partial charges of the adsorbates and the adsorbents

Atom	ε/k_B [K]	σ [Å]	Charge [e⁻]
N(NO$_2$) [29]	50.36	3.24	0.146
O(NO$_2$) [29]	62.51	2.93	-0.073
N (N$_2$O$_4$)[29]	50.36	3.24	0.588
O(N$_2$O$_4$) [29]	62.51	2.93	-0.294
Si (Zeo) [68]	22.00	2.30	1.50
O (Zeo) [68]	53.00	3.30	0.75

Five pure-silica zeolites with different geometry and topology are selected, considering them as rigid frameworks. Despite the well-known fact that the effect of zeolite flexibility could play a role on the diffusion of the molecules in the structure, this effect is usually small in adsorption studies.[70] Besides, diffusion results achieved using flexibility strongly depend on the model used.[71] A representation of the grid surface energy of the selected materials can be seen in Fig. 1. MOR, TON, FER, and MFI are zeolites with a structure consisting of interconnected channels with different directionality. Crystallographic position of the atoms of zeolite MOR are taken from the work of Gramlich.[72] This zeolite is formed by parallel channels in the *z*-axis with additional adsorption sites in the *y*-axis. The so-called side pockets are accessible from the main channels only for small molecules.[17] TON zeolite, whose atomic positions are taken from Marler,[73] also has a 1D system of channels, but without pockets associated. The channels in MOR are made of 12-member rings, while TON has 10-member rings, resulting in limiting diameters of about 6.5 Å and 5 Å, respectively. FER shows a 2-dimensional intersected system of channels of 4.7 Å (10-member rings in the *z*-axis) and 3.4 Å (8-member rings in the *y*-axis).[74] 10-members rings also configure the main

channels of MFI zeolite (*x*-axis), which are intersected by zig-zag secondary channels leading to a 3-dimensional system with limiting diameters around 4.5-4.7 Å.[75] The last zeolite under study, FAU, has a cubic cell with two types of interconnected cages.[76] The biggest cages, α-cages, are accessible through a 12-member ring window. The smallest, β-cages or sodalites, are connected by 6-member rings windows but are not accessible for most of the molecules due to the narrow windows that connect them with the α-cages (4-meber rings). To comply with the experimental conditions, cavities that are not accessible for the molecules under study need to be blocked.[77,78] As in a previous work, we use Monte Carlo and Molecular Dynamics simulations to identify these inaccessible cavities.[79] The first, identifies energetic preferential adsorption sites, while the second informs about the diffusion of the molecules. These sites from which molecules are unable to escape after 0.15 ns were properly blocked. In RASPA, the blockage is implemented using a list of geometric descriptions of the inaccessible volumes that are automatically considered as an overlap in MC simulations. Using this methodology, sodalites in FAU and *y*-axis channels in FER were identify and blocked due to narrow access windows that do not allow diffusion of both molecules under study, considering FER zeolite as 1-dimensional framework for them. A summary of some other interesting properties of the structures, such as surface area, pore size distributions, and pore volume, are computed for later analysis (Table S1 and Fig. S1 in the ESI.).
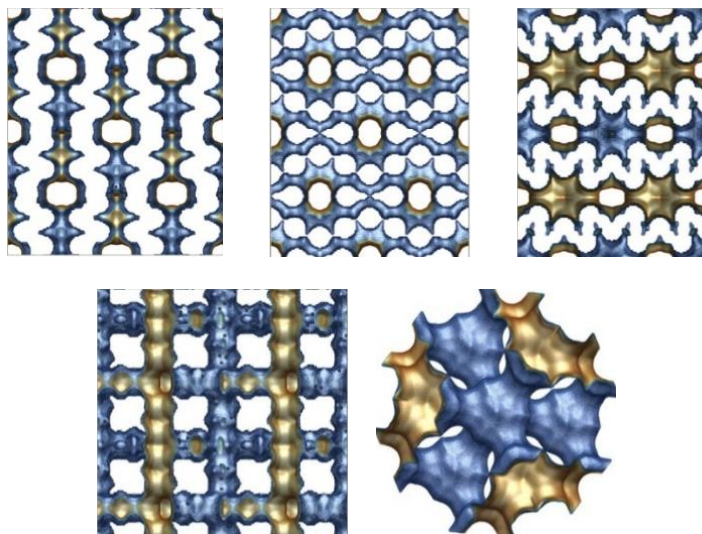
Fig. 1 Energy grid surface of zeolites MOR, TON, and FER (top) and MFI and FAU (down). The accessible surface is colored in brown and the inaccessible surface in blue.

Results and Discussion

Bulk-phase reaction

To validate molecular models taken from the literature and the partition functions calculated in this work, we carried out RxMC simulations in the isothermal-isobaric (NPT) ensemble for the bulk phase dimmer destruction reaction ($N_2O_4 \leftrightarrow NO_2$). Equilibrium constant for thee reaction is defined in this work as eq. 4.

$$K_{P\,[atm]} = \frac{P_{NO_2}^2}{P_{N_2O_4}} = \frac{(P_{Total} \cdot X_{NO_2})^2}{P_{Total} \cdot X_{N_2O_4}} \qquad (4)$$

K_P is the equilibrium constant, P_{Total} is the system total pressure, and $P_{i,j}$ and $X_{i,j}$ are the partial pressures and the mole fractions of each species respectively. Equilibrium constants for reaction over a temperature range of 273-404 K, are shown in Table 4, comparing experimental, calculated, and simulated results. Original experimental values were obtained by Wourtzel,[35] Bodenstein and Boës,[34] and Verhoek and Daniels.[31] The values listed in the table were recalculated by Giauque and Kemp.[36] Calculated constants were obtained by Chao *et al.* from derivation of thermodynamic functions[32] and our

13

results were obtained in this work at 1 atm of total pressure. The obtained equilibrium constants are in agreement with data from other authors for the full range of temperatures. Fig. 2 shows the equilibrium mole fraction of N_2O_4 over the studied range of temperatures at pressures from 0.1 to 5 atm. The reference data from the figure were obtained from Chao *et al.*[32] for 0.1 and 1 atm and extrapolated to 0.5 and 5 atm using reported equilibrium constants. In the figure, simulated results also describe very well the N_2O_4 equilibrium mole fractions in the full range of temperature and pressure. As expected from experimental evidence, high temperatures favor the destruction of the N_2O_4 dimer molecules. Focusing on the results obtained at ambient pressure, the N_2O_4 mole fraction remains above 0.6 up to room temperature. At higher temperatures, the mole fraction strongly decreases up to less than 0.1 at around 360 K, being almost negligible above 370 K. Increase in pressure has a reverse effect, increasing the fraction of dimer at a fixed temperature. For example, at room temperature N_2O_4 fraction is increased from c.a. 0.3 to c.a. 0.8 from 0.1 to 5 atm, respectively. Information from Fig. 2 is summarized in Table S2 in the ESI. Having validated the equilibrium compositions in the bulk phase using our simulations, we study the equilibrium reaction in the pore phase.

Table 4 Comparison of experimental and calculated equilibrium constants for the N_2O_4-NO_2 system. Our data were obtained at 1 atm.

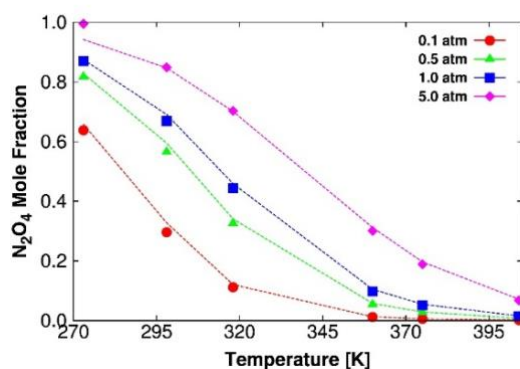| T [K]	K_P [atm]		
	Exp.[36]	Calc.[32]	This work.
273.10	0.018	0.018	0.019
298.10	0.136	0.146	0.162
318.10	0.628	0.621	0.688
359.60	7.499	7.487	8.239
374.68	16.180	16.111	17.484
403.93	59.430	60.354	63.485

Fig. 2 Mole fraction of N₂O₄ for the bulk phase reaction dimerization over a temperature range of 273-404 K and a pressure range of 0.1-5 atm. Solid symbols depict the results obtained in this work from RxMC simulations in the NPT ensemble and dashed line show calculated data from Chao *et al.*[32] for direct comparison.

Pure component and equimolar binary mixture adsorption isotherms from GCMC simulations

Pure component adsorption isotherms and equimolar binary mixture of NO_2 and N_2O_4 at room temperature are shown in Fig. 3**.** The reaction trial move is switched off here. We compute these isotherms in hypothetical pure and equimolar mixture compositions to analyze the adsorption performance of each molecule as a previous stage for further discussion of equilibrium mixtures and reaction itself. Pure component adsorption isotherms in Fig. 3a show that NO_2 starts to adsorb in the zeolites at 10 kPa, with loadings at ambient pressure of around 0.5-1 $mol \cdot kg^{-1}$. The lowest loading at this pressure was found for FAU, the zeolite with the largest pore diameter and cavities (see Table and Fig. S1 in the ESI) in which NO_2 molecules are less strongly bound due to energy effects.[80–82] Saturation loadings are not reached at the highest pressure under study (10^3 kPa), showing uptakes ordered as a function of the available pore volume of the zeolites: c.a. 1.5 $mol \cdot kg^{-1}$ (FER and TON), c.a. 2.5 $mol \cdot kg^{-1}$ (MOR and MFI), and c.a. 3.5 $mol \cdot kg^{-1}$ (FAU). Dinitrogen tetroxide adsorption in MFI takes place at 10^{-2}-10^{-1} kPa, three orders of

magnitude of pressure lower than the monomer, and saturation loading (c.a. 2 mol·kg^{-1}) is reached at 1 kPa. In the rest of zeolites adsorption initiates at 10^{-1}-10^{0} kPa and saturation is almost reach at 10-10^{2} kPa, with loadings c.a 1-1.5 mol·kg^{-1} (FER, TON and MOR) and 5 mol·kg^{-1} (FAU). As for NO_2, saturation loadings are ordered as a function of the total pore volume (FAU > MFI > TON > FER), with MOR as exception. Fig. 4 shows the NO_2 and N_2O_4 Average Occupation Profiles (AOP) in zeolite MOR (more detailed views of the distribution of these molecules can be found in Fig. S2 and S3 in the ESI). As observed from the figure, while the monomer is absorbed both in the main straight channels and the side pockets, the adsorption of the dimer only takes place in the channels. Part of its pore volume (side pockets) is not accessible for N_2O_4, explaining why the saturation loading of the dimer in MOR is lower compared to MFI (with similar pore volume), being closer to the saturation values of TON, which have similar topology but without side pockets and lower pore volume than MOR. Adsorption isotherms from equimolar binary mixture are shown in Fig. 3b. The adsorption of N_2O_4 is almost unaffected by the presence of NO_2. Some reduction in loading can be observed at low-medium pressure caused by the fact that the feeder gas stream now contains 50% of each species, but this effect disappears at saturation, with similar loadings than in the pure component isotherms. On the contrary, the adsorption of NO_2 is strongly influenced by the presence of dimers. When N_2O_4 is present in the system, the adsorption of NO_2 drastically decreases to almost negligible values. This behavior occurs in all zeolites except for MOR. In this zeolite, the loading of monomers is reduced about 1 mol·kg^{-1}, but with similar N_2O_4 saturation loading, meaning no NO_2 favorable competition for the adsorption sites in the main channels of the structure. As expected from the distribution of molecules as pure components inside this zeolite, the remaining NO_2 adsorption in the equimolar mixture takes places only in the side pockets, where there is no competition

with N_2O_4 (see AOP in Fig. S2-S3 in the ESI). The presence of these adsorption sites makes a difference in the adsorption performance compared to other structures with very similar topology such as TON or FER, in which the adsorption of monomers is completely displaced from the channels with no alternative adsorption sites.
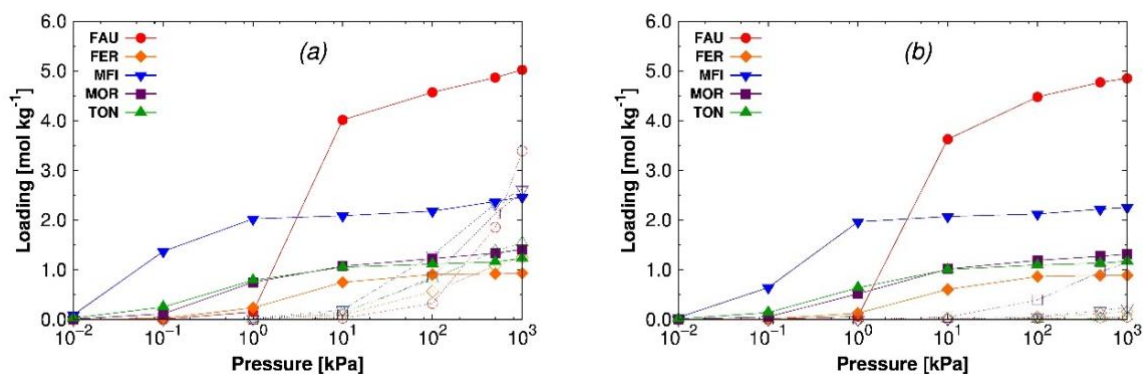

Fig. 3 Calculated pure components (a) and binary equimolar mixture (b) adsorption isotherms of NO_2 (empty symbols) and N_2O_4 (full symbols) at room temperature in FAU (red circles), FER (orange diamonds), MFI (blue down triangles), MOR (purple squares), and TON (green triangles). Reaction trial moves are switched off here.
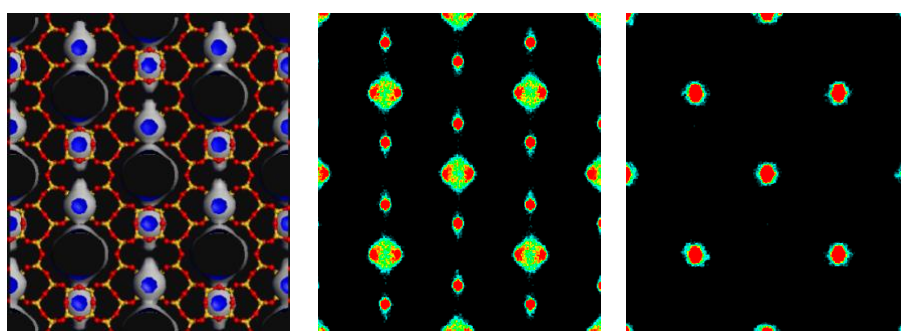

Fig. 4 Average Occupation Profiles of NO_2 (center) and N_2O_4 (right) in zeolite MOR at $5\cdot10^2$ kPa and room temperature. The figure shows the projection of the center of mass of the molecules over the *x-y* plane. The color gradation (from black to red) indicates the occupation density. To guide the view, a representation of the structure is added (left)

where oxygen atoms are depicted in red and silica atoms in yellow. A grid surface is also represented where the accessible part is colored in blue and the non-accessible part in gray.

Bulk-equilibrium binary mixtures

The effect of confinement in the equilibrium mixture containing NO_2 and N_2O_4 is also studied. Adsorption isotherms over an extended range of pressures ($10^{-1} - 10^3$ kPa) are obtained at troom temperature. Isobars at 10^2 and $5 \cdot 10^2$ kPa at temperatures spanning from 260 K and 420 K are also calculated.

Adsorption Isotherms. Adsorption results from reactive grand-canonical Monte Carlo simulations for the N_2O_4/NO_2 equilibrium mixture at room temperature are shown in Fig. 5. Fig. 5a shows the NO_2 and N_2O_4 adsorption isotherms from equilibrium binary mixtures and Fig. 5b show the adsorbed mole fraction of N_2O_4 on the zeolites. The composition of the bulk phase at equilibrium was obtained from NPT reactive MC simulations and used to fix the GCMC bulk-phase composition (also depicted in Fig. 5b to guide the discussion). Additionally, results obtained using reactive GCMC are compared to these obtained from reactive constant pressure Gibbs ensemble simulations in Fig. S4 in the ESI. We compare results obtained from different methodologies to ensure that the two of them lead to the same results. The agreement using the two approaches allow us to use reactive GCMC simulations for the rest of the study taking advantage of its lower computational cost in comparison with GE-NPT in which both phases need to be simulated at the same time for each simulation.[47]

In Fig. 5a we see similar behavior as for the observed from the equimolar binary mixture, with some minor differences. At pressure below $3 \cdot 10^1$ kPa, the mole fraction of

N_2O_4 in the bulk is lower than this of NO_2 and the adsorption of N_2O_4 is softly reduced compared to the equimolar binary mixture. The starting adsorption of dimers is displaced one order of magnitude in pressure (from 10^{-1} to 1 kPa) in FER, TOR, and MOR while the loading in MFI is reduced 1 mol·kg^{-1} at the same pressure. The adsorption in FAU initiates at the same pressure (1 kPa) but the loading at 10 kPa is also reduce about 1 mol·kg^{-1}. At values of pressure above $3·10^1$ kPa, the ratio between the mole fractions of NO_2 and N_2O_4 is reversed and mole fraction of N_2O_4 becomes larger than this of NO_2. Saturation loadings are reached in all the zeolites above 10^2 kPa, as described in binary equimolar mixture. The adsorption of NO_2 at low pressure is almost negligible despite its larger proportions in the bulk phase, and at high pressure the low NO_2 fraction in the bulk phase reduces the number of molecules adsorbed in the side pockets of MOR, the only structure in which there is competition with N_2O_4 in equimolar conditions.

The mole fractions of dinitrogen tetroxide as a function of pressure depicted in Fig. 5b corroborate that confinement goes in favor of dimerization in the full range of pressure. Results at very low pressure (10^{-1} kPa) should be ignored since lodgings are almost negligible for the two adsorbates. In MFI, important loading is reached at 1 kPa (c.a. 1 mol·kg^{-1}) being the NO_2 adsorbed fraction almost negligible. From this pressure, N_2O_4 adsorbed fraction reaches almost 1.0 as NO_2 adsorption is avoided by N_2O_4 molecules in most zeolites. In relation to the influence of zeolite topology on the equilibrium composition of the reaction mixture, MFI shows the strongest influence. This zeolite has one of the narrowest system of channels under study and interconnections where molecules tend to be preferentially absorbed. TON and MOR are the next two structures with the highest N_2O_4 adsorbed fractions at low pressure, being 1D structures with slightly bigger channels than MFI. FAU is the zeolite where both species commensurate worst. Its high available pore volume and its topology consisting of big cages, weaken

the confinement of the gas molecules. Finally, the performance of FER can be attributed to the fact that the secondary system of channels of this zeolite is not accessible for the studied molecules and the available pore volume is the smallest among the studied zeolites. Therefore, this structure has the lowest N_2O_4 adsorption at low and high pressure. Focusing on MOR, the adsorption behavior considering the mole fractions of both components as a function of pressure is particularly interesting. At low pressures, the adsorbed fraction of dimers is larger than the bulk mole fraction, as happens for the other zeolites. However, once the monomers start entering the side pockets, the trend is inverted. Fig. 5b shows that the adsorbed mole fraction of dimers is lower than the bulk fraction at pressure above 10^2 kPa. This is due to the adsorption of NO_2 molecules in the side pockets of this zeolite, where there is no competition with dimer molecules in spite of its progressive reduction in the bulk phase.
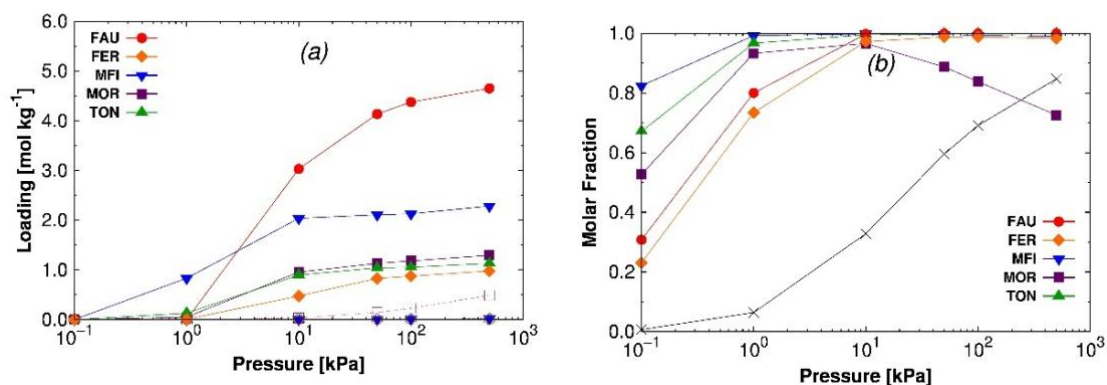

Fig. 5 Calculated binary mixture adsorption isotherms (a), and mole fractions (b) of NO_2 (open symbols) and N_2O_4 (closed symbols) at room temperature in FAU (red circles), FER (orange diamonds), MFI (blue down triangles), MOR (purple squares), and TON (green triangles). To clear the figure and guide the eye in (b), only the N_2O_4 mole fractions are plotted (the sum of both mole fractions is equal to 1) and the bulk mole fractions

(obtained from NPT reactive simulations) are also added in black. Reaction move is switched on here.

The adsorption selectivity of N_2O_4 over NO_2 is shown in Fig. 6. We defined the adsorption selectivity of component i over component j (S_{ij}) as $(x_i/y_j)/(x_j/y_j)$ where $x_{i,j}$ are the mole fractions in the adsorbed phase and $y_{i,j}$ the mole fractions in the bulk phase.[83] The figure shows that the selectivity up to 10 kPa (before saturation of the pore space) follows the same order than described in Fig. 5b (MFI > TON > MFI > FAU > FER). This means that is strongly related to the order in which N_2O_4 is adsorbed in the zeolites. At 10 kPa FAU shows a high increase in both loading and selectivity showing the best performance at high pressure. Around 10^1-10^2 kPa, N_2O_4 reaches saturation and the loading does not increase despite its bulk fraction keeps increasing for increasing values of pressure, resulting on a reduction of the selectivity but not a significant modification on the adsorbed amount of each component, as can be seen in Fig. 5a. This reduction is particularly important in MOR, being the selectivity inverted towards NO_2 above 10^2 kPa because the main channels are already saturated of N_2O_4 and the amount of NO_2 adsorbed in the side pockets still increases while the NO_2 bulk fraction decreases.
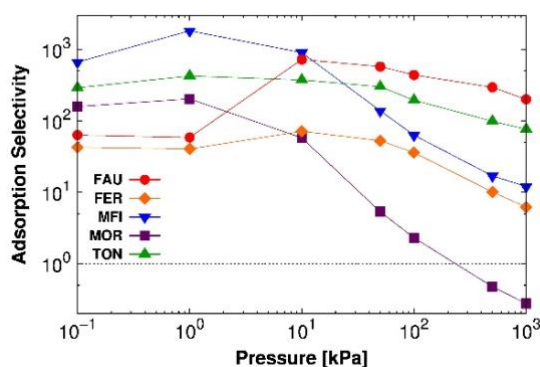

Fig. 6 Adsorption selectivity N_2O_4/NO_2 from the binary equilibrium mixture at room temperature in FAU (red circles), FER (orange diamonds), MFI (blue down triangles),

MOR (purple squares), and TON (green triangles). Dotted line in the figure denotes an inversion in the selectivity from a N_2O_4 selective behavior to a NO_2 selective behavior. Reaction move is switched on here.

Summarizing, confinement favors the formation of dimers at any pressure at room temperature, increasing its mole fraction regardless the bulk phase concentration. However, structural features have to be taken into account carefully as they are able to invert this behavior. This happens in zeolite MOR, where there are sites only accessible for NO_2 which makes them very sensitive to the existence of this species in the gas mixture in contraposition with the rest of zeolites in which NO_2 can be ignored.

Adsorption Isobars. The effect of temperature in the confined equilibrium mixture is analyzed in Fig. 7 at temperatures ranging from 260 K to 400 K. Fig. 7a depicts NO_2 and N_2O_4 adsorbed isobars at room pressure. Dinitrogen tetroxide shows saturation loadings in almost all zeolites below 320 K, with a reduction above this temperature due to a combined effect between the increment on the movement of the particles and the decrease of the N_2O_4 bulk fraction. This reduction is more remarkable in FAU as this zeolite has the highest pore volume and diameter, and N_2O_4 does not fit as tightly as in the other zeolites. Around 370 K only MFI keeps a loading of about a half of its total capacity, while at the highest temperature the loading is almost negligible in all zeolites. The adsorption of NO_2 is very low in all zeolites, even in MOR in which also the side pockets are poorly occupied at temperature below 320 K (less than 0.5 mol·kg^{-1}). No increase in the NO_2 adsorbed amount can be seen when NO_2 bulk fraction increases with temperature, probably due to a very low pressure preventing NO_2 adsorption. Adsorption isobars at $5·10^2$ kPa are depicted in Fig. 7b. At this pressure, the decrease in the adsorbed

amount of N_2O_4 at temperature above 320 K is softer than at room pressure, and slightly higher loadings appear at high temperature. The pressure increase does not affect the NO_2 adsorption at low temperatures in most zeolites due to the low mole fraction in the bulk composition. MOR is the exception since the adsorption of NO_2 in the side pockets is increased by pressure increase at low temperatures. In this zeolite, the NO_2 isobar shows a linear behavior as a result of the balanced effect that the temperature exerts on the adsorption performance of this compound. On the one hand, for increasing temperature the bulk fraction of monomer increases. On the other hand, the entropic effect and so the adsorption is reduced at higher values of temperature. In the other zeolites, the increment of NO_2 in the bulk fraction with temperature is also responsible of the small rise in its loading at the highest temperature, in contraposition with the decrease of the dimer adsorption.
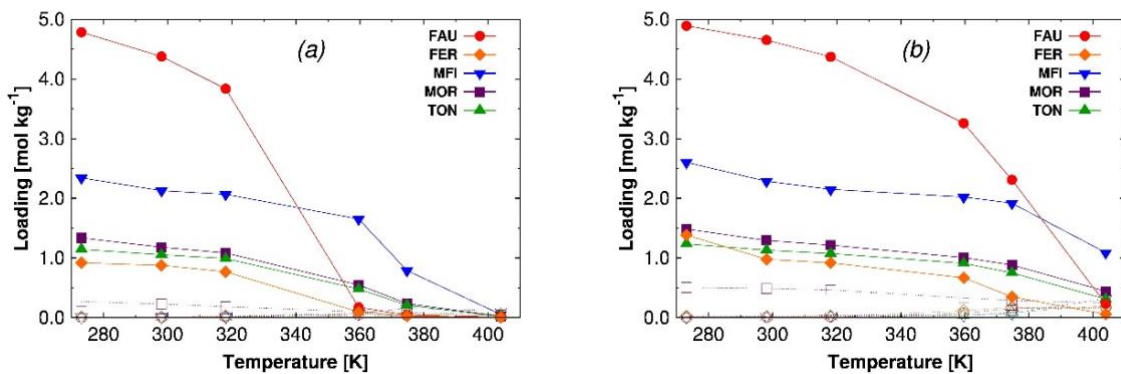

Fig. 7 Calculated binary mixture adsorption isobars of NO_2 (empty symbols) and N_2O_4 (full symbols) at 10^2 (a) and $5 \cdot 10^2$ kPa (b) in FAU (red circles), FER (orange diamonds), MFI (blue down triangles), MOR (purple squares), and TON (green triangles). Reaction move is switched on here.

Adsorbed dinitrogen tetroxide mole fraction from equilibrium mixture as a function of temperature is depicted in Fig 8. To see the effect of confinement in the mole fraction and

to guide the discussion, the bulk fraction obtained from NPT reactive simulations is also depicted in the figure. At ambient pressure (Fig. 8a), the adsorption of N_2O_4 prevails over NO_2 in the full range of temperature, showing larger fraction of adsorbed dinitrogen tetroxide than in the bulk. Below 320 K, N_2O_4 fractions near 1 can be observed in all zeolites except MOR, in which they are near 0.8 due to the adsorption of NO_2 in the side pockets. Above this temperature, the reduction in the N_2O_4 loading (Fig. 7a) is responsible for the reduction of the N_2O_4 adsorbed fraction. For increasing pressure to $5 \cdot 10^2$ kPa, the reduction of N_2O_4 adsorption at 320 K is not so remarkable as at room pressure because of a stronger N_2O_4 adsorption. The behavior at low pressure is similar for most zeolites, but in this case, MOR shows a reduction on the N_2O_4 adsorbed fraction compared to the bulk. Despite the fact that the adsorption of monomers in MOR takes place at the two different pressures in this study, the adsorption is lower at ambient pressure, as it is a low value of pressure for NO_2 to be properly adsorbed. At ambient pressure, the adsorbed amount of dimer is larger than the expected compared to the bulk phase, with a mole fraction about 20% reduced respect to other zeolites up to 320 K. On the contrary, at the highest value of pressure the adsorbed mole fraction of N_2O_4 is lower than in the bulk phase up to 320 K, confirming that MOR is very sensitive to the presence of NO_2, whose initial bulk fraction is lower than 0.10-0.25 between 280-320 K. For increasing temperature, the increase of monomer mole fraction in combination with the reduction of the total loading adsorbed, reduces and finally eliminates this effect, making this structure more selective to N_2O_4.
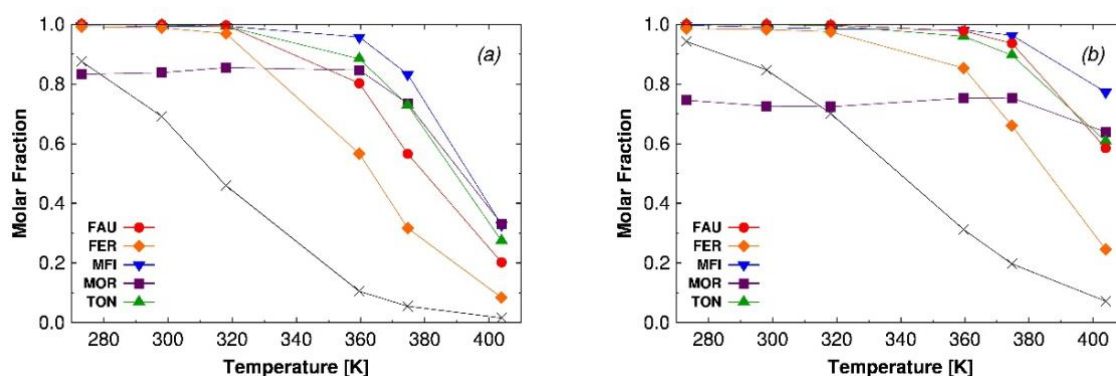
Fig. 8 Calculated binary mixture N_2O_4 adsorbed mole fractions at (a) 10^2 and (b) $5 \cdot 10^2$ kPa in FAU (red circles), FER (orange diamonds), MFI (blue down triangles), MOR (purple squares), and TON (green triangles). To guide the view, the N_2O_4 bulk mole fraction, obtained from NPT reactive simulations, is also added in black. Reaction move is switched on here.

Conclusions

We use molecular simulations to study the effect of confinement of equilibrium mixtures containing nitrogen dioxide and dinitrogen tetroxide. Models taken from literature and partitions functions calculated in this work were validated by reproducing previously published equilibrium constants and mole fractions of the components in the bulk phase. We verified that the increase of temperature favors the destruction of N_2O_4, while pressure has the opposite effect. The study of pure component and equimolar mixtures at room temperature shows that the interaction with all zeolites is stronger for N_2O_4 than for NO_2, being absorbed 2-3 orders of magnitude in pressure before and reaching saturation loadings at room pressure. Saturation is not reached in the range of pressure under study for NO_2 in any of the zeolites, and its adsorption was drastically

reduced to almost negligible values when introducing N_2O_4 in the system. However, MOR keep a remarkable NO_2 loading due to the existence of special adsorption sites for this molecule where N_2O_4 did not fit. When analyzing adsorption isotherms and isobars of the reacting mixture in the zeolites, confinement was proved to be responsible for the formation of dimers in the full range of pressure and temperature. Increased density of the adsorbates in the pore phase compared to bulk, as well the N_2O_4 selective behavior of the zeolites, are responsible for the N_2O_4 formation. The largest deviations from bulk concentrations were found at low temperatures and high pressures, as the effect of confinement weakens at high temperatures and low pressures due to a decrease in the difference in the adsorption strength of both molecules. Among the studied zeolites, MFI exerts the most noticeable influence in the equilibrium composition since is a zeolite with one of the narrowest system of channels accessible for the molecules, closely followed by TON and MOR. On the other hand, the low available pore volume of FER and the wide size of the cages in FAU, reduce the effect of confinement in these two zeolites. In addition, selective adsorption sites for NO_2 molecules in MOR strongly modified the general behavior, allowing a high adsorption selectivity towards NO_2 at low temperatures and high pressure. These findings demonstrate that the topological structure of confined systems, such as zeolites, has a crucial influence on the composition of the mixture. General behavior, N_2O_4 formation in this case, can be modified at certain conditions of pressure and temperature by special structure features such as side-pockets in MOR, as Kim *et al.* already observed for CO_2/CH_4 separation.[84] These features must be carefully considered and highlight the need of paying special attention when managing NO_2 adsorption and removal from computational screenings and experimental studies.

Conflicts of interest

There are no conflicts to declare.

References and Notes

1   K. Mollenhauer and H. Tschöke, *Handbook of Diesel Engines*, Springer Berlin Heidelberg, New Delhi, 1st edn., 2010.

2   H. Omidvarborna, A. Kumar and D. S. Kim, *Fuel Process. Technol.*, 2015, **140**, 113–118.

3   L. Sloss, *Nitrogen Oxides Control Technology Fact Book*, 1992.

4   B. Son, W. Yang, P. Breysse, T. Chung and Y. Lee, *Environ. Res.*, 2004, **94**, 291–296.

5   A. K. Das, J. D. Wilde, G. J. Heynderickx and G. B. Marin, *Aiche J.*, 2001, **47**, 2831–2844.

6   X. L. Zhang, D. O. Hayward, C. Lee and D. M. P. Mingos, *Appl. Catal. B-Environmental*, 2001, **33**, 137–148.

7   V. Sanchez-Escribano, T. Montanari and G. Busca, *Appl. Catal. B Environ.*,

2005, **58**, 19–23.

8   P. Forzatti and L. Lietti, *Heterog. Chem. Rev.*, 1996, **3**, 33–51.

9   M. Shelef, *Chem. Rev.*, 1995, **95**, 209–225.

10   E. de Visser, C. Hendriks, M. Barrio, M. J. Mølnvik, G. de Koeijer, S. Liljemark
       and Y. Le Gallo, *Int. J. Greenh. Gas Control*, 2008, **2**, 478–484.

11   L. F. Ding and A. O. Yazaydin, *J. Phys. Chem. C*, 2012, **116**, 22987–22991.

12   J. Yu, Y. Ma and P. B. Balbuena, *Langmuir*, 2012, **28**, 8064–8071.

13   I. Matito-Martos, A. Martin-Calvo, J. J. Gutiérrez-Sevillano, M. Haranczyk, M.
       Doblare, J. B. Parra, C. O. Ania and S. Calero, *Phys. Chem. Chem. Phys.*, 2014,
       16, 19884--19893.

14   H. Deng, H. Yi, X. Tang, Q. Yu, P. Ning and L. Yang, *Chem. Eng. J.*, 2012, **188**,
       77–85.

15   Y. Wang, Z. Huang, Z. Liu and Q. Liu, *Carbon N. Y.*, 2004, **42**, 445–448.

16   Y. Liu, T. M. Bisson, H. Yang and Z. Xu, *Fuel Process. Technol.*, 2010, **91**,
       1175–1197.

17   E. Garcia-Perez, J. B. Parra, C. O. Ania, A. Garcia-Sanchez, J. M. Van Baten, R.
       Krishna, D. Dubbeldam and S. Calero, *Adsorpt. Int. Adsorpt. Soc.*, 2007, **13**,
       469–476.

18   M. P. Bernal, J. Coronas, M. Menendez and J. Santamaria, *AIChE J.*, 2004, **50**,
       127–135.

19   J. P. Anerousis, *Chem. Eng.*, 1976, **83**, 128.

20   C. Baerlocher, L. B. McCusker and D. H. Olson, *Atlas of Zeolite Framework
       types*, Elsevier, London, 6th edn., 2007.

21   W. Sun, L. C. Lin, C. Peng and B. Smit, *AIChE J.*, 2014, **60**, 2314–2323.

22   L.-C. Lin, A. H. Berger, R. L. Martin, J. Kim, J. A. Swisher, K. Jariwala, C. H. Rycroft, A. S. Bhown, M. Deem, M. Haranczyk and B. Smit, *Nat. Mater.*, 2012, **11**, 633–641.

23   B. Smit and T. L. M. Maesen, *Chem. Rev.*, 2008, **108**, 4125–4184.

24   V. Lachet, B. Creton, T. de Bruin, E. Bourasseau, N. Desbiens, Ø. Wilhelmsen and M. Hammer, *Fluid Phase Equilib.*, 2012, **322–323**, 66–78.

25   A. L. Smith and H. L. Johnston, *J. Amer. Chem. Soc*, 1952, **74**, 4696–4698.

26   H. J. R. Guedes, Universidade Nova de Lisboa, 1988.

27   E. D. Glendening and A. M. Halpern, *J. Chem. Phys.*, 2007, **127**, 164307.

28   F. Kohler, *J. Mol. Liq.*, 1995, **67**, 105–123.

29   E. Bourasseau, V. Lachet, N. Desbiens, J.-B. Maillet, J.-M. Teuler and P. Ungerer, *J. Phys. Chem. B*, 2008, **112**, 15783–15792.

30   K. Yoshino, J. R. Esmond and W. H. Parkinson, *Chem. Phys.*, 1997, **221**, 169–174.

31   F. H. Verhoek and F. Daniels, *J. Am. Chem. Soc.*, 1931, **53**, 1250–1263.

32   J. Chao, R. C. Wilhoit and B. J. Zwolinski, *Thermochim. Acta*, 1974, **10**, 359–371.

33   D. W. James and R. C. Marshall, *J. Phys. Chem.*, 1968, **72**, 2963–2966.

34   M. Bodenstein and F. Boës, *Z. Phys. Chem. A*, 1922, **100**, 75.

35   E. Wourtzel, *C. R. Acad. Sci. Paris*, 1919, **169**, 1397–1400.

36   W. F. Giauque and J. D. Kemp, *J. Chem. Phys.*, 1938, **6**, 40–51.

37   L. Harris and L. K. Churney, *J. Chem. Phys.*, 1967, **47**, 1703–1709.

38   J. K. Johnson, A. Z. Panagiotopoulos and K. E. Gubbins, *Mol. Phys.*, 1994, **81**, 717–733.

39   W. R. Smith and B. Triska, *J. Chem. Phys.*, 1994, **100**, 3019–3027.

40   C. Heath Turner, J. K. Brennan, M. Lísal, W. R. Smith, J. Karl Johnson and K. E. Gubbins, *Mol. Simul.*, 2008, **34**, 119–146.

41   H. C. Turner, K. J. Johnson and K. E. Gubbins, *J. Chem. Phys.*, 2001, **114**, 1851–1859.

42   L. Pusztai, H. Dominguez and O. A. Pizio, *Rev. Mex. Fis.*, 2003, **49**, 212–218.

43   J. Carrero-Mantilla and M. Llano-Restrepo, *Fluid Phase Equilib.*, 2006, **242**, 189–203.

44   H. Dominguez and O. A. Pizio, 2002, **316**, 65–76.

45   M. Lísal, W. R. Smith and I. Nezbeda, *AIChE J.*, 2000, **46**, 866–875.

46   M. Borówko and R. Zagórski, *J. Chem. Phys.*, 2001, **114**, 5397–5403.

47   N. Hansen, S. Jakobtorweihen and F. J. Keil, *J. Chem. Phys.*, 2005, **122**, 164705.

48   S. Jakobtorweihen, N. Hansen and F. J. Keil, *J. Chem. Phys.*, 2006, **125**, 224709.

49   R. G. Mullen and E. J. Maginn, *J. Chem. Theory Comput.*, 2017, acs.jctc.7b00498.

50   D. A. McQuarrie and J. D. Simon, *Physical Chemistry: a molecular approach*, University Science Books: Sausalito, California, 1 st ed., 1997.

51   A. Poursaeidesfahani, R. Hens, A. Rahbari, M. Ramdin, D. Dubbeldam and T. J. H. Vlugt, *J. Chem. Theory Comput.*, 2017, acs.jctc.7b00092.

52   S. P. Balaji, S. Gangarapu, M. Ramdin, A. Torres-Knoop, H. Zuilhof, E. L. V

Goetheer, D. Dubbeldam and T. J. H. Vlugt, *J. Chem. Theory Comput.*, 2015, **11**, 2661–2669.

53   D. R. Stull and H. Prophet, *JANAF thermochemical tables, No. NSRDS-NBS-37*, National Standard Reference Data System, 1971.

54   T. W. Rosch and E. J. Maginn, *J. Chem. Theory Comput.*, 2011, **7**, 269–279.

55   M. J. Frisch, G. W. Trucks, H. B. Schlegel, G. E. Scuseria, M. A. Robb, J. R. Cheeseman, G. Scalmani, V. Barone, G. A. Petersson, H. Nakatsuji, X. Li, M. Caricato, A. Marenich, J. Bloino, B. G. Janesko, R. Gomperts, B. Mennucci, H. P. Hratchian, J. V. Ortiz, A. F. Izmaylov, J. L. Sonnenberg, D. Williams-Young, F. Ding, F. L. F. Egidi, J. Goings, B. Peng, A. Petrone, T. Henderson, D. Ranasinghe, V. G. Zakrzewski, J. Gao, N. Rega, G. Zheng, W. Liang, M. Hada, M. Ehara, K. Toyota, R. Fukuda, J. Hasegawa, M. Ishida, T. Nakajima, Y. Honda, O. Kitao, H. Nakai, T. Vreven, K. Throssell, J. A. Montgomery, J. E. Peralta, F. Ogliaro, M. Bearpark, J. J. Heyd, E. Brothers, K. N. Kudin, V. N. Staroverov, T. Keith, R. Kobayashi, J. Normand, K. Raghavachari, A. Rendell, J. C. Burant, S. S. Iyengar, J. Tomasi, M. Cossi, J. M. Millam, M. Klene, C. Adamo, R. Cammi, J. W. Ochterski, R. L. Martin, K. Morokuma, O. Farkas, J. B. Foresman and D. J. Fox, *Gausian 09 Revision C.02*, Gaussian Inc., Wallingford CT, 2016.

56   G. Herzber, *Molecular spectra and molecular structure. Volume 3: Electronic spectra and electronic structure of polyatomic molecules*, Van Nostrand, New Jersey, 1966.

57   T. Shimanouchi, *J. Phys. Chem. Ref. Data*, 1977, **6**, 993–1102.

58   L. M. S. E. P. Kraǐnov and M. A. Kovner, *Vibrational spectra of polyatomic*

molecules, New York, 1974.

59   J. L. Domenech, A. M. Andrews, S. P. Belov, G. T. Fraser and W. J. Lafferty, *J. Chem. Phys.*, 1994, **100**, 6993.

60   M. E. Jacox, *Vibrational and Electronic Energy Levels of Polyatomic Transient Molecules, Journal of Physical and Chemical Reference Data (Book 3)*, American Institute of Physics, 1994.

61   A. Stirling, I. Pápai, J. Mink and D. R. Salahub, *J. Chem. Phys.*, 1994, **100**, 2910.

62   M. W. Chase, 1996, **25**, 551–601.

63   M. W. Chase, J. L. Curnutt, H. Prophet, R. A. McDonald and A. N. Syverud, *J. Phys. Chem. Ref. Data*, 1975, **4**, 1–176.

64   D. Frenkel and B. Smit, *Understanding Molecular Simulations: From Algorithms to Applications*, C. Academic Press, San Diego, CA, second edi., 2002.

65   M. P. Allen, D. J. Tildesle and D. J. Tildesley, *Computer Simulation of Liquids*, Oxford University Press, Oxford, Second Edi., 2017.

66   D. Dubbeldam, S. Calero, D. E. Ellis and R. Q. Snurr, *Mol. Simul.*, 2015, **42**, 81–101.

67   D. Dubbeldam, A. Torres-Knoop and K. S. Walton, *Mol. Simul.*, 2013, **39**, 1253–1292.

68   P. Bai, M. Tsapatsis and J. I. Siepmann, *J. Phys. Chem. C*, 2013, **117**, 24375–24387.

69   M. P. Allen and D. J. Tildesley, *Computer Simulation of Liquids*, Oxford Clarendon Press, Oxford, 1987.

70   T. J. H. Vlugt and M. Schenk, *J. Phys. Chem. B*, 2002, **106**, 12757–12763.

71   A. Garcia-Sanchez, D. Dubbeldam and S. Calero, *J. Phys. Chem. C*, 2010, **114**, 15068–15074.

72   V. Gramlich, Ph.D. Thesis, ETH, Zürich, Switzerland, 1971.

73   B. Marler, *Zeolites*, 1987, **7**, 393–397.

74   R. E. Morris, S. J. Weigel, N. J. Henson, L. M. Bull, M. T. Janicke, B. F. Chmelka and A. K. Cheetham, *J. Am. Chem. Soc.*, 1994, **116**, 11849–11855.

75   H. van Koningsveld, H. van Bekkum and J. C. Jansen, *Acta Crystallogr. Sect. B-Structural Sci.*, 1987, **43**, 127–132.

76   J. J. A. Hriljac, M. M. M. Eddy, A. K. K. Cheetham, J. A. A. Donohue and G. J. J. Ray, *J. Solid State Chem.*, 1993, **106**, 66–72.

77   S. Calero, D. Dubbeldam, R. Krishna, B. Smit, T. J. H. Vlugt, J. F. M. Denayer, J. A. Martens and T. L. M. Maesen, *J. Am. Chem. Soc.*, 2004, **126**, 11377–11386.

78   R. Krishna and J. M. van Baten, *Langmuir*, 2010, **26**, 2975–2978.

79   I. Matito-Martos, J. Álvarez-Ossorio, J. J. Gutiérrez-Sevillano, M. Doblaré, a. Martin-Calvo and S. Calero, *Phys. Chem. Chem. Phys.*, 2015, **17**, 18121–18130.

80   R. Krishna and J. M. van Baten, *Phys. Chem. Chem. Phys.*, 2011, **13**, 10593–10616.

81   R. Krishna, B. Smit and S. Calero, *Chem. Soc. Rev.*, 2002, **31**, 185–194.

82   A. Torres-Knoop and D. Dubbeldam, *ChemPhysChem*, 2015, **16**, 2046–2067.

83   J. Talbot, *AIChE J.*, 1997, **43**, 2471–2478.

84   J. Kim, M. Abouelnasr, L.-C. Lin and B. Smit, *J. Am. Chem. Soc.*, 2013, **135**, 7545–7552.

ADSORPTION EQUILIBRIUM OF NITROGEN DIOXIDE AND DINITROGEN TETROXIDE IN POROUS MATERIALS

I. Matito-Martos[a], A. Rahbari[b], A. Martin-Calvo[c], D. Dubbeldam[d], T.J.H. Vlugt[b], and S. Calero[*a]

[a]*Department of Physical, Chemical and Natural Systems, University Pablo de Olavide, Sevilla 41013, Spain*

[b]*Process and Energy Department, Delft University of Technology, Leeghwaterstraat 39, 2628CB Delft, The Netherlands*

[c]*Department of Chemical Engineering, Vrije Universiteit Brussel, Brussels, 1050, Belgium*

[d]*Van 't Hoff Institute for Molecular Sciences, University of Amsterdam, Science Park 904, 1098XH Amsterdam, The Netherlands*

Supporting Information

Table S1 Structural and topological properties of the zeolites under study.

Zeolite	Pore Volume (cm3g)	Surface area (m^2/g)	Density (kgm3)	Channel System	Channel Diameter	Channel Diameter	Channel Diameter	Ring sizes
FER	0.066	235.07	1837.87	2D (1D)	4.69	3.4	-	10 8 6 5
TON	0.091	301.41	1968.716	1D	5.11	-	-	10 6 5
MOR	0.15	477.92	1711.056	1D	6.45	-	-	12 8 5 4
MFI	0.164	547.67	1796.342	3D	4.7	4.46	4.46	10 6 5 4
FAU	0.332	1020.88	1342.047	3D - Cages	7.35	7.35	7.35	12 6 4

Table S2 Mole fraction of NO_2 and N_2O_4 for the bulk phase reaction dimerization over a temperature range of 273-404 K and a pressure range of 0.1-5 atm. The table shows the results obtained in this work from RxMC simulations in the NPT ensemble and calculated data from Chao et al.[32] for direct comparison.

| Pt [atm] = 0.1					Pt [atm] = 0.5				
	Mole Fraction		Mole Fraction[32]			Mole Fraction		Mole Fraction[32]	
T [K]	NO_2	N_2O_4	NO_2	N_2O_4	T [K]	NO_2	N_2O_4	NO_2	N_2O_4
273	0.362	0.638	0.342	0.658	273	0.183	0.817	0.172	0.828
298	0.704	0.296	0.672	0.328	298	0.435	0.565	0.405	0.595
318	0.888	0.112	0.879	0.121	318	0.674	0.326	0.659	0.341
360	0.988	0.012	0.987	0.013	360	0.946	0.054	0.942	0.058
375	0.994	0.006	0.994	0.006	375	0.973	0.027	0.971	0.029
404	0.998	0.002	0.998	0.002	404	0.992	0.008	0.992	0.008
Pt [atm] = 1					Pt [atm] = 5				
	Mole Fraction		Mole Fraction[32]			Mole Fraction		Mole Fraction[32]	
T [K]	NO_2	N_2O_4	NO_2	N_2O_4	T [K]	NO_2	N_2O_4	NO_2	N_2O_4
273	0.13	0.87	0.125	0.875	273	0.005	0.995	0.058	0.942
298	0.331	0.669	0.309	0.691	298	0.151	0.849	0.153	0.847
318	0.556	0.444	0.541	0.459	318	0.297	0.703	0.299	0.701
360	0.902	0.098	0.895	0.105	360	0.699	0.301	0.688	0.312
375	0.949	0.051	0.945	0.055	375	0.811	0.189	0.803	0.197
404	0.985	0.015	0.984	0.016	404	0.932	0.068	0.928	0.072
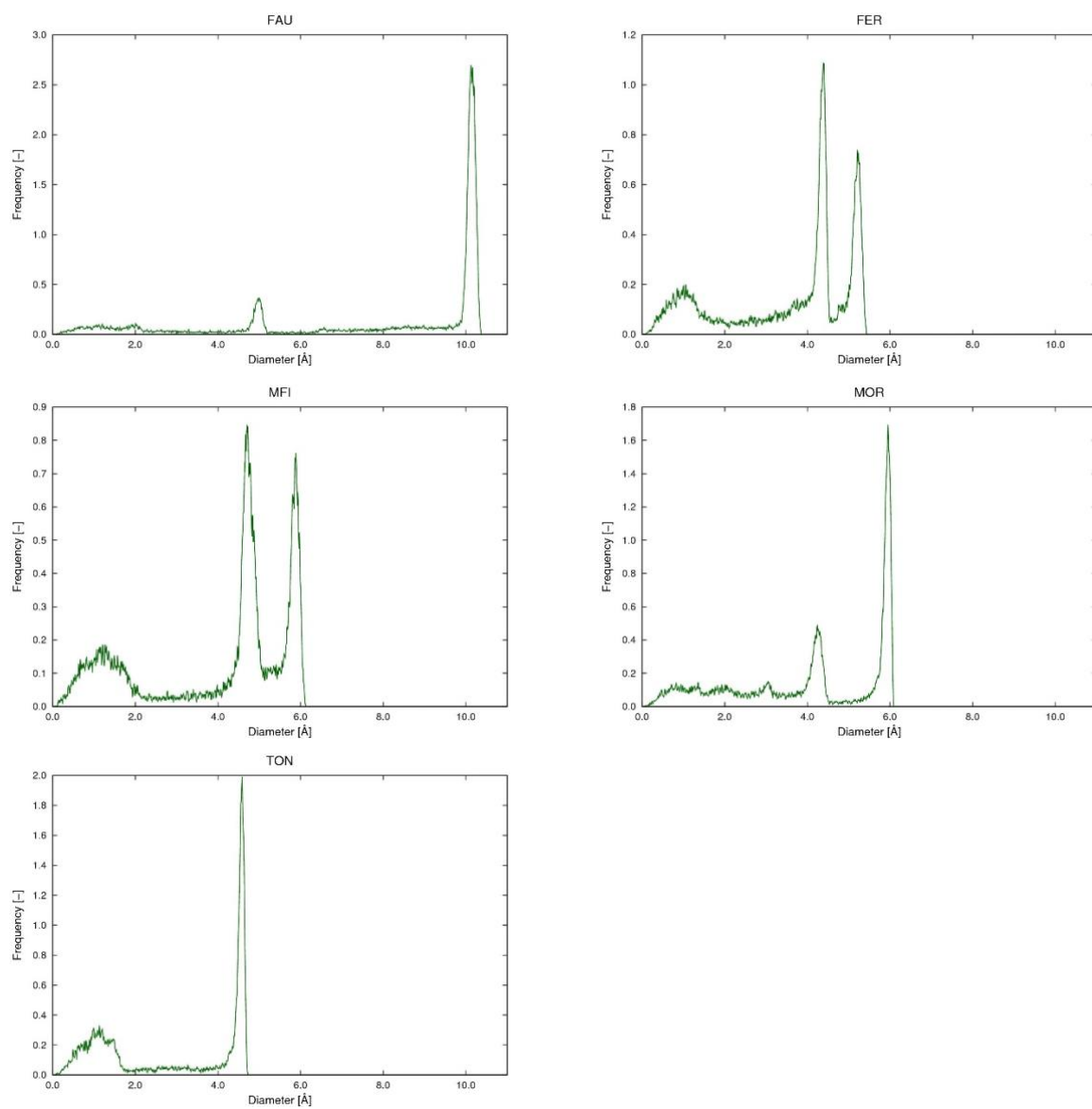
Fig. S1 Pore-size distributions of the zeolites under study (from top left to bottom right: FAU, FER, MFI, MOR, and TON).
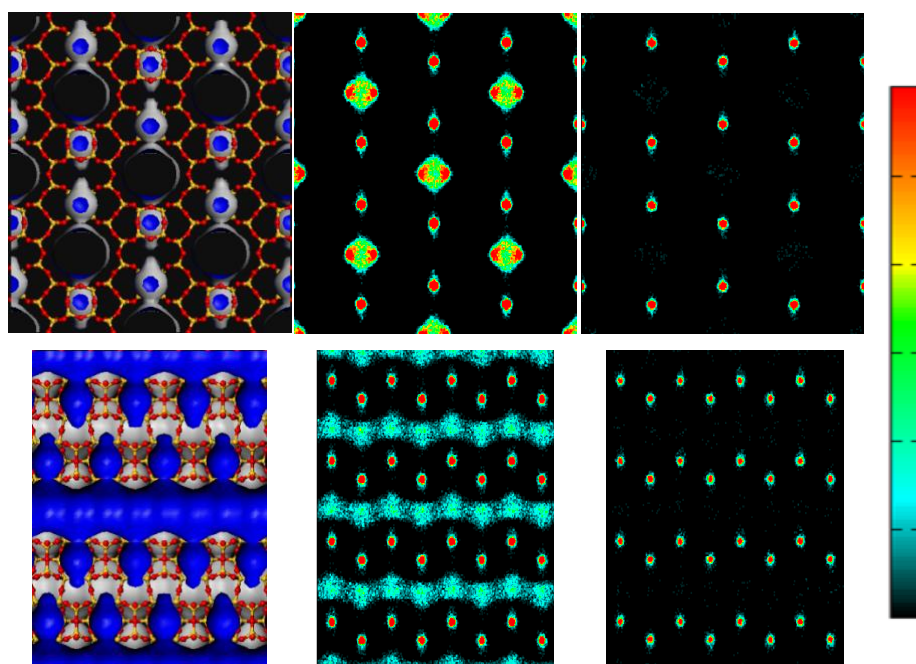
Fig. S2 Average occupation profiles for nitrogen dioxide in MOR zeolite at $5 \cdot 10^2$ kPa and room temperature, obtained from pure component (central column) and binary equimolar mixture NO_2-N_2O_4 (right column). The figures show the projection of the center of mass of the molecules over the x-y (top) and z-y (bottom) planes. The color graduation indicates the occupation density (from black to red). To guide the view a representation of the structure (left column) is added (oxygen atoms are depicted in red and silica atoms in yellow). A grid surface is also represented where the accessible part appears in blue while the non-accessible part is colored in gray.
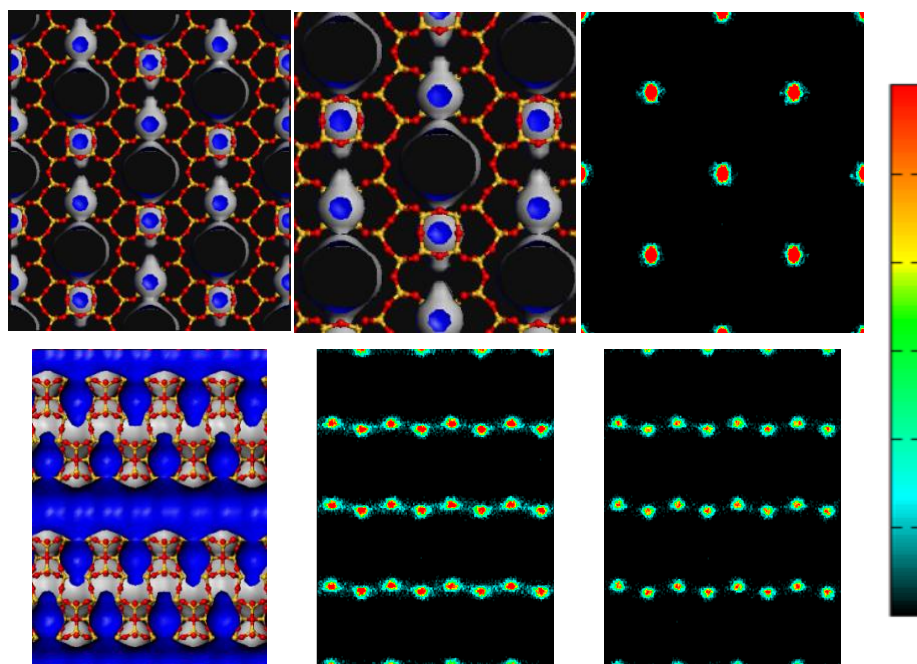
Fig. S3 Average occupation profiles for dinitrogen tetroxide in MOR zeolite obtained from pure component at room pressure (central column) and binary equimolar mixture NO_2-N_2O_4 at 10^3 kPa (right column) and room temperature in both cases. The figures show the projection of the center of mass of the molecules over the x-y (top) and z-y (bottom) planes. The color graduation indicates the occupation density (from black to red). To guide the view a representation of the structure (left column) is added (oxygen atoms are depicted in red and silica atoms in yellow). A grid surface is also represented where the accessible part appears in blue while the non-accessible part is colored in gray.
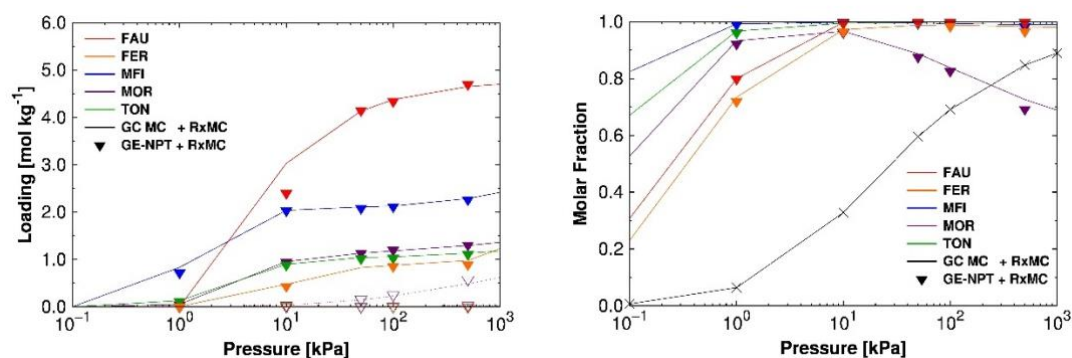
Fig. S4 Simulated binary mixture adsorption isotherms (left), and mole fractions (right) of NO_2 (empty symbols) and N_2O_4 (full symbols) at room temperature in FAU (red), FER (orange), MFI (blue down triangles), MOR (purple squares), and TON (green triangles). In both figures, results obtained using reactive Grand-Canonical Monte Carlo simulation are depicted as line and those obtained from constant pressure Gibbs ensemble reactive simulations as down pointed triangles. To clear the figure and guide the eye in (right), only the N_2O_4 mole fractions are plotted (the sum of both mole fractions is equal to 1) and the bulk mole fractions are also added in black. Reaction move is switched on here.